PROCEEDINGS

PCF 2014

XIV Portuguese Conference on Fracture

UNIVERSIDADE DE TRÁS-OS-MONTES E ALTO DOURO

utad

PROCEEDINGS

EDITED BY

Abílio de Jesus

Alfredo Ribeiro

José Morais

José Xavier

Nuno Dourado

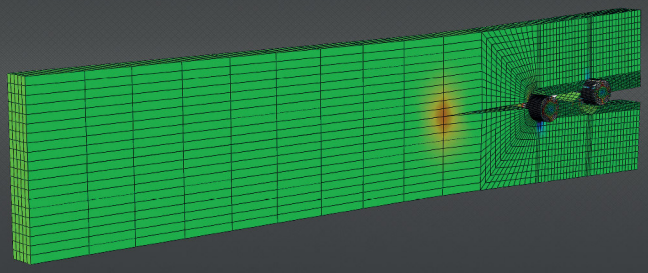

RÉGUA, 6-7TH FEBRUARY, 2014

PCF 2014

XIV Portuguese Conference on Fracture

DIRECT METHOD FOR DETERMINING THE COHESIVE LAW OF PINUS PINASTER IN MODE I BY DIGITAL IMAGE CORRELATION

J. Xavier[1,*], J.M. Oliveira[1,2], P. Monteiro[1], J.J.L. Morais[1], M.F.S.F. de Moura[3]

[1] University of Trás-os-Montes e Alto Douro, UTAD, CITAB, Quinta de Prados, 5000-801 Vila Real, Portugal.
[2] DEMad, ESTG, Polytechnic Institute of Viseu, 3504-510, Viseu, Portugal.
[3] DEMec, FEUP, University of Porto, Rua Dr. Roberto Frias, 4200-465 Porto, Portugal.

ABSTRACT

The direct identification of the cohesive law in pure mode I of *Pinus pinaster* is addressed. The approach couples the double cantilever beam (DCB) test with digital image correlation (DIC). Wooden beam specimens loaded in the radial-longitudinal (RL) fracture propagation system are used. The strain energy release rate in mode I (G_I) is uniquely determined from the load-displacement (P–δ) curve by means of the compliance-based beam method (CBBM). This method relies on the concept of equivalent elastic crack length (a_{eq}) and therefore does not require the monitoring of crack propagation during test. The crack tip opening displacement in mode I w_I is determined from the displacement field at the initial crack tip. The cohesive law in mode I (σ_I–w_I) is then identified by numerical differentiation of the G_I–w_I relationship. The methodology and accuracy on this reconstruction are addressed. Moreover, the proposed procedure is validated by finite element analyses including cohesive zone modelling. It is concluded that the proposed data reduction scheme is adequate for assessing the cohesive law in pure mode I of *P. pinaster*.

KEYWORDS: Wood; Mode I fracture mechanics; Double cantilever beam test; Cohesive law; Digital image correlation.

1. INTRODUCTION

Wood is a hierarchical, anisotropic and heterogeneous composite material formed by trees. Recently, green composites based on lignocellulosic fibres and forest-based resources have attracted increasing interest in both research and market [1,2]. Moreover, in a policy of sustainability, wood and wood products are increasingly used nowadays, for instance, in structural and semi-structural applications [3]. However, for a better and efficient utilisation of wood material, several issues must be further investigated. One fundamental aspect concerns the fracture mechanical behaviour of wood.

Relatively extensive fracture process zones (FPZ) are observed in wood due to fibre bridging and micro-cracking ahead of the crack tip [4]. However, the microstructural mechanisms in wood fracture are usually confined to a region of reduced thickness [5]. Therefore, at the macroscopic scale, the wood behaviour in the FPZ can be conveniently described through a phenomenological constitutive cohesive law [6,7]. In order to obtain the cohesive law, one approach consists in minimising an objective function quantifying the difference between numerical and experimental load-displacement ($P-\delta$) curves by inverse analysis, assuming a given shape of the softening law. This approach, however, is semi-empirical and does not guarantee the uniqueness of the solution. Notwithstanding, it has been shown that the inverse identification of cohesive laws provide good agreement between experimental and numerical finite element simulations [7,8]. Instead, a direct method for evaluating the cohesive law can be proposed based on independent determination of strain energy release rate and crack tip opening displacement (CTOD) [9]. The advantages of this approach are: (i) the shape of the cohesive law does not need to be assumed a priori; (ii) the cohesive law is determined based on local measurements.

In this work, a direct identification of the cohesive law in mode I of *P. pinaster* was investigated by coupling the double cantilever beam (DCB) test with digital image correlation (DIC). Specimens oriented in the radial-longitudinal (RL) propagation system were used. The strain energy release rate in mode I (G_I) was explicitly determined from the $P-\delta$ curve by means of the compliance-based beam method (CBBM). This data reduction scheme is based on the concept of equivalent elastic crack length (a_{eq}) and, therefore, does not require the measurement of the crack length during test. An independent evaluation of CTOD in mode I (w_I) was determined from displacement fields at the initial crack tip. The direct differentiation of the G_I-w_I curve and the reconstruction of the σ_I-w_I cohesive law, by means of least-squares regression using a continuous approximation function, were

* Corresponding author. Tel.: +351 259 350 356; fax: +351 259 350 356.
E-mail address: jmcx@utad.pt

addressed. The proposed procedure was also validated by finite element simulations including cohesive zone modelling.

2. DATA REDUCTION

The DCB test is schematically shown in Fig. 1. The specimen is a $L_1 \times 2h \times B$ mm^3 rectangular beam. The resistance curve (*R*–curve) can then be determined from the Irwin-Kies equation

$$G_{\mathrm{I}} = \frac{P^2}{2B}\frac{\mathrm{d}C}{\mathrm{d}a} \tag{1}$$

in which $C = \delta / P$ is the compliance. From the Timoshenko beam theory and Castigliano theorem an expression for the compliance of the DCB specimen can be obtained. This equation can be solved for the flexural modulus (E_f) using an initial compliance (C_0) and the corrected initial crack length ($a_0 + \Delta$) as

$$E_f = \left(C_0 - \frac{12(a_0+\Delta)}{5BhG_{\mathrm{LR}}} \right)^{-1} \frac{8(a_0+\Delta)^3}{Bh^3} \tag{2}$$

where Δ can be determined from finite element analysis and G_{LR} is the shear moduli of the material. The CBBM is based on a_{eq}, which is considered to account for the FPZ effect at the crack tip as given by: $a_{\mathrm{eq}} = a + \Delta + \Delta a_{\mathrm{FPZ}}$ [7,10]. Finally, the application of CBBM to the DCB test yield the following expression for the strain energy release rate in mode I (resistance or *R*–curve)

$$G_{\mathrm{I}} = \frac{6P^2}{B^2 h}\left(\frac{2a_{\mathrm{eq}}^2}{E_f h^2} + \frac{1}{5G_{\mathrm{LR}}} \right). \tag{3}$$

It is worth noting that this procedure is less sensitive to experimental errors such as crack length monitoring and inherent variability of elastic properties.

In mode I loading, strain energy release rate (G_{I}) and CTOD (w_{I}) can be related by the following expression [9]

$$G_{\mathrm{I}} = \int_o^{w_{\mathrm{I}}} \sigma_{\mathrm{I}}(\overline{\mathrm{w}}_{\mathrm{I}})\,\mathrm{d}\overline{\mathrm{w}}_{\mathrm{I}} \tag{4}$$

The cohesive law ($\sigma_{\mathrm{I}} = \mathrm{f}(w_{\mathrm{I}})$) can then be directly obtained by differentiating the above equation

$$\sigma_{\mathrm{I}}(w_{\mathrm{I}}) = \frac{\partial G_{\mathrm{I}}}{\partial w_{\mathrm{I}}}. \tag{5}$$

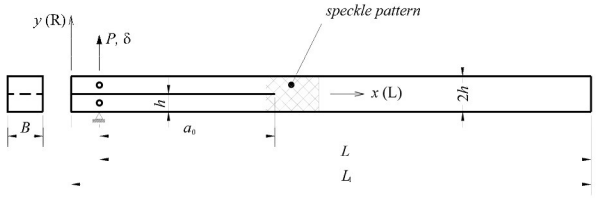

Fig. 1. Schematic representation of the DCB test $2h$ = 20 mm, L_1 = 300 mm, L = 280 mm, B = 20 mm and a_0 = 100 mm).

This data reduction scheme, however, requires the accurate evaluation of the $G_{\mathrm{I}} = \mathrm{f}(w_{\mathrm{I}})$ relationship. Moreover, a suitable differentiation algorithm must be used to avoid noise amplification in the reconstruction of the constitutive cohesive law. In order to solve Eq. (5), it is proposed here to fit the $G_{\mathrm{I}} - w_{\mathrm{I}}$ data by a continuous function described by the following expression (logistic function)

$$G_{\mathrm{I}} = \frac{A_1 - A_2}{1 + (w_{\mathrm{I}} / w_{\mathrm{I},0})^p} + A_2 \tag{6}$$

where A_1, A_2, p and $w_{\mathrm{I},0}$ are constants to be determined in least-square sense. In this function, the A_2 parameter must provide an estimation of the critical strain energy release rate: $A_2 = \lim_{w_{\mathrm{I}} \to \infty} G_{\mathrm{I}} = G_{\mathrm{Ic}}$.

In the literature, several analytical expressions for the cohesive law in mode I have been proposed. Among them, there is the Xu and Needleman exponential law [11]

$$\sigma_{\mathrm{I}} = \frac{G_{\mathrm{Ic}}}{w_{\mathrm{Iu}}}\left(\frac{w_{\mathrm{I}}}{w_{\mathrm{Iu}}} \right) \exp\left(\frac{w_{\mathrm{I}}}{w_{\mathrm{Iu}}} \right). \tag{7}$$

in which w_{Iu} is the crack tip opening displacement at maximum stress (σ_{Iu}) (see cohesive law in Fig. 2). The logistic (Eq. 6) and exponential (Eq. 7) cohesive laws are then compared and discussed during the analysis.

3. DIGITAL IMAGE CORRELATION

Full-field optical techniques have become very important tool in experimental solid mechancis. Among them, DIC has become widely used, following the development of digital cameras and automatic digital image processing techniques [12]. This computer vision technique has the advantages of a simple principle and experimental set-up, which can switch from large down to small scales of observation. In DIC-2D, a planar object is imaged by a single camera-lens optical system connected to a computer for real-time visualisation. It is assumed that the surface of interest has a local random textured pattern uniquely characterising the material surface. A matching process is then carried out between images taken before and after deformation. Typically, the reference (undeformed) image is divided into

subsets, whose number of pixels defines the displacement spatial resolution (*i.e.*, the smaller distance separating two independent displacement measurements). The selection of these measuring parameters, together with the quality of the speckle pattern, are key issues for determining the spatial resolution and accuracy associated to DIC measurements. Therefore, they should be carefully chosen in a compromise between correlation (small subsets) and interpolation (large subsets) errors.

3.1 CRACK TIP OPENING DISPLACEMENT

The CTOD in mode I (w_1) was determined by processing the displacements provided by DIC. For a complex material such as wood, this technique can be advantageous with regard to standard monitoring procedures. As a procedure, the initial crack length is firstly identified in the reference (undeformed) image. A suitable pair of subsets near the crack tip is then selected. During the test, the relative displacement of these points is evaluated. The w_1 can then be determined by [13,14]

$$w_1 = \left\| w_1^+ - w_1^- \right\| \tag{8}$$

where w_1^+ and w_1^- are the components of the displacement in the direction perpendicular to the crack propagation associated to the upper and the lower cracked surface and $\|.\|$ represent the Euclidean norm.

4. FINITE ELEMENT SIMULATION

Two-dimensional finite element analyses (FEA) of the DCB test, including cohesive zone modelling, were performed in ABAQUS in order to validate the proposed procedure using CBBM. Nominal dimensions of the DCB specimen were (Fig. 1): $2h$ = 20 mm, L_1 = 300 mm, L = 280 mm, B = 20 mm and a_0 = 100 mm. Isoparametric 8-node planar solid finite elements (CPS8R) were used for the bulk material, whilst 6-node cohesive elements were applied along the FPZ, which in this case was confined to a line at mid-height of the specimen (Fig. 2). Wood was modelled as an orthotropic linear elastic material [7,15-17].

5. EXPERIMENTAL WORK

Specimens for the DCB test were cut from a single *P. pinaster* tree. Matched specimens were selected in the mature region within the stem. Twelve specimens were prepared with axes oriented along the RL propagation system. The nominal dimensions of the DCB specimens were those already used in the numerical simulation (Fig. 1).

The fracture tests were performed in an INSTRON 1125 universal testing machine, with a controlled cross-head displacement rate of 3 mm/min. The load was measured by means of a 5 kN load cell, setting the gain at 50 N/V. Specimens were tested after stabilisation at laboratory conditions of 60-65% relative humidity and temperature of 20-25 ºC.

The ARAMIS DIC-2D system was used in this work [18]. The speckled pattern required in the DIC method was painted over the region of interest by means of an airbrush to guarantee suitable granulometry, contrast and isotropy at the scale of magnification.

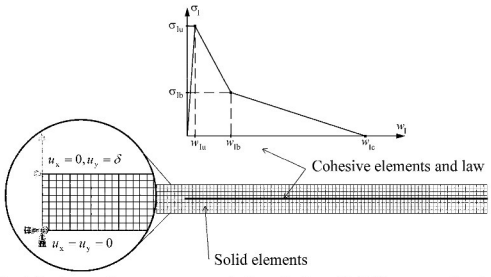

Fig. 2. Finite element model of the DCB test (cohesive law, mesh and boundary conditions).

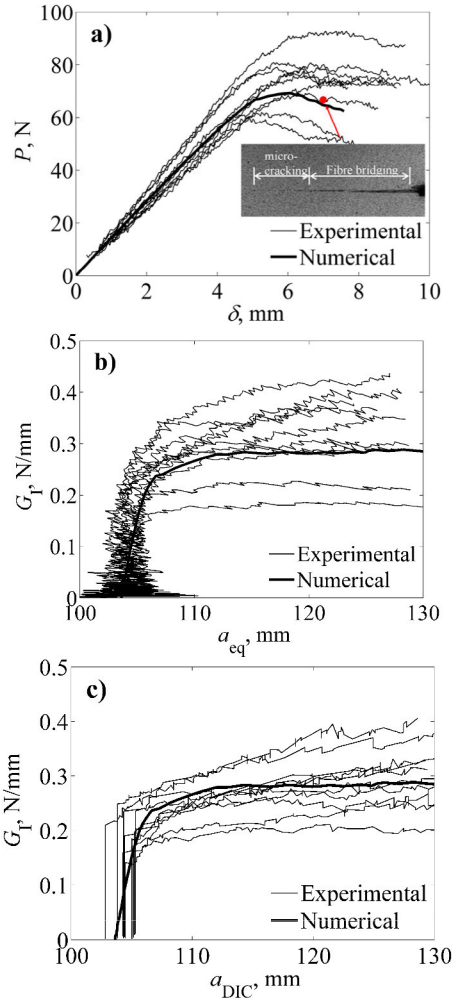

Fig. 3. DCB test: (a) curves and macroscopic visualization of the crack propagation; (b) *R*–curve obtained by CBBM; (c) *R*–curve obtained by Irwin-Kies equation

For DIC analyses, a subset size of 15×15 pixel^2 (0.270×0.270 mm^2) and a subset step of 13×13 pixel^2 (0.234×0.234 mm^2) were selected for enhancing spatial

resolution [19]. A resolution in displacement and strain of a and was respectively obtained. For measuring CTOD (w_I), the coordinates of the initial crack tip were firstly identified in the reference image. The w_I was then determined by post-processing the displacement of subsets chosen upper and lower the crack tip during the test (Eq. 8). The base distance between the two subsets was 0.468 mm.

6. RESULTS AND DISCUSSION

The crack length propagation during the fracture test was determined based on DIC measurements: $a_{DIC}(\delta) = a_0 + \Delta a(\delta)$. The algorithm proposed for this evaluation together with a further comparison between a_{eq} and a_{DIC} as a function of the applied displacement in the DCB test is described in detailed in [10]. Hereafter, a systematic evaluation of mode I fracture properties (R – curve and cohesive law) obtained from both CBBM and Irwin-Kies equations is addressed. To start with, the R–curves determined from both Irwin–Kies equation and CBBM (Eq. 3) were analysed. The compliance versus crack length (a_{DIC}) function was fitted in the least-square sense by a cubic function of the form: $C = ma^3 + n$. The analytical differentiation of this function was then used in order to compute G_I. Fig. 3a shows the $P-\delta$ curves obtained experimentally together with the numerical one resulting from FEA using the trilinear cohesive law (Fig. 1). The scatter on the initial compliance among the curves ($C_0 = 0.072 \pm 0.0076$ mm/N) is expected due to the inherent variability of the material. Moreover, qualitatively, the numerical prediction of the $P-\delta$ curve was in good agreement with the experimental ones. In Fig. 3a it is also shown a macroscopic visualisation of crack propagation. As it can be seen, micro-cracking and fibre bridging can be identified. This confirms the difficulties in measuring accurately the crack length using conventional monitoring techniques. Some authors (e.g., [20]) report that the main mechanism of mode I fracture is fibre bridging. However, these observations suggest that both micro-cracking and fibre bridging contribute significantly for the energy dissipation in the FPZ. The R–curves in mode I obtained from the DCB test by both CBBM and Irwin-Kies equations are shown in Fig. 3b and 3c, respectively, together with the numerical resistance curve. The wide dispersion of the experimental curves is most likely a reflection of the local variability of wood microstructure at the initial crack tip (e.g., earlywood and latewood constituents).

From the R–curves, the evaluation of the strain energy release rate in mode I was carried out at two distinct stages. The first corresponds to the starting point of the non-linearity in the $P-\delta$ curve and therefore the initialisation of the FPZ (G_{Ii}), whilst the second is defined at the maximum loading (G_{Im}). Due to the fact that some of the R–curves do not reveal a clear plateau identifying the critical strain energy release rate, it was assumed that: $G_{Im} = G_{Ic}$. This value is then related to the complete development of the FPZ and initial steady-state crack propagation. The G_{Ii} and G_{Ic} values for both CBBM and Irwin-Kies equations are reported in Table 1, together with density and flexural modulus (Eq. 2). These results point out that an underestimation of G_I can be obtained if the actual crack length is used (Eq. 1) because a fraction of fracture energy dissipation at the FPZ is not properly taken into account. It should be noted that the density values among specimens have a coefficient of variation (C.V.) lower than 4%. Consequently, it is not surprising that scatter of G_{Ii} and G_{Ic} was not statistically correlated with density. Indeed, as already pointed out, this scatter is likely due to natural variability of wood cellular structure at the crack tip among specimens. As can be concluded, the evaluation of the strain energy release rate in mode I by the Irwin-Kies equation is slightly lower than the one from CBMM. This difference is of 11.7% and 12.9% for G_{Ii} and G_{Ic} respectively, which is lower than the coefficients of variation among the tested specimens.

From the DIC measurements both normal and transverse CTOD, with regard to the crack plane, were determined during the DCB test. As expected, CTOD in mode II (w_{II}) was negligible. Characteristic R–curves in mode I ($G_I - w_I$) were then obtained as shown in Fig. 4a and Fig. 5a for the CBBM and Irwin-Kies equations, respectively. The numerical characteristic R–curve obtained by FEA of the DCB test was generically in relative good agreement with the experimental ones. For determining the cohesive law (Eq. 5), a logistic function (Eq. 6) was firstly fitted to the experimental data as shown in Figs. 4b (CBBM) and 5b (Irwin-Kies). For this analysis, only the data points just before initial crack propagation, where the FPZ is assumed to be completely developed were considered. As it can be seen, a relatively good approximation was obtained in both cases. This procedure allows filtering experimental data and provides a basis for analytical differentiation, which is less prone to noise amplification. The cohesive laws in mode I obtained from the DCB test are shown in Figs. 4c (CBBM) and 5c (Irwin-Kies), together with the numerical curve.

The parameters (A_1, A_2, p and $w_{I,0}$) of the logistic function (Eq. 6) obtained from this study are reported in Tables 2 (CBBM) and 3 (Irwin-Kies), together with the characteristic values of maximum stress (σ_{Iu}) and relative displacements (w_{Iu}, w_{Ic} in Fig. 2) in mode I. The mean value of A_2 (Tables 2 and 3) represents an estimation of G_{Ic} and it is in agreement with the independent measurements based on the R–curves (Table 1). It is interesting to notice that σ_{Iu} (Tables 2,

Table 1. Density (ρ), flexural modulus (E_f), initial (G_{Ii}) and critical (G_{Ic}) strain energy release rates in mode I obtained from the DCB tests by CBBM and Irwin-Kies (IK) equation.

Specimens	ρ	E_f	CBBM		IK	
			G_{Ii}	G_{Ic}	G_{Ii}	G_{Ic}
	(g/cm^3)	(N/mm^2)	(N/mm)	(N/mm)	(N/mm)	(N/mm)
1	0.539	9888	0.22	0.41	0.18	0.34
2	0.566	7279	0.14	0.28	0.10	0.21
3	0.529	8890	0.10	0.18	0.15	0.25
4	0.545	7423	0.14	0.41	0.14	0.40
5	0.548	8585	0.20	0.30	0.18	0.27
6	0.550	9833	0.17	0.29	0.15	0.27
7	0.535	7585	0.13	0.21	0.12	0.19
8	0.496	8473	0.20	0.37	0.16	0.30
9	0.566	8043	0.25	0.34	0.20	0.27
10	0.553	10105	0.17	0.27	0.15	0.25
Mean	0.543	8610	0.17	0.31	0.15	0.27
C.V.(%)	3.8	12.2	26.3	25.4	18.6	22.1

3) is of the same order of magnitude as the radial tensile strength (7.93 MPa) measured from tensile tests on *P. pinaster* (with density of 0.7 g/cm^3) in [21].

The mean cohesive law in mode I for *P. pinaster* was determined from the mean values of the parameters governing the logistic function, as shown in Figs. 4d (CBBM) and 5d (Irwin-Kies). For comparison purposes, the exponential (Eq. 7) cohesive law is also plotted in Figs. 4d (CBBM) and 5d (Irwin-Kies), determined from mean values of the fitting parameters. Qualitatively both laws have a similar behaviour as summarised in Tables 2 and 3.

7. CONCLUSIONS

The resistance curves in mode I of *P. pinaster* were determined by applying the CBBM and Irwin-Kies equations to the DCB fracture test. Initial and critical strain energy release rates in mode I were then determined. These values are in agreement with reference values reported in the literature for this wood species. By combining the strain energy release rates, determined from both CBBM and Irwin-Kies equations, with CTOD in mode I provided by DIC, characteristic *R*–curves and cohesive laws in mode I for *P. pinaster* were evaluated by the direct method. Results were consistent with literature values. Moreover, the proposed procedure was validated by finite element simulations using a cohesive zone model.

8. REFERENCES

1. Satyanarayana K, Arizaga GGC, Wypych F (2009) Biodegradable composites based on lignocellulosic fibers – An overview. Prog Polym Sci 34(9):982–1021
2. Xavier J, Belini U, Pierron F, Morais J, Lousada J, Tomazello M (2013) Characterisation of the bending stiffness components of MDF panels from full-field slope measurements. Wood Sci Technol 47(2):423–441
3. FAO (2009) State of the World's Forests 2009 Report. Part 2 - Adapting for the future. UN Food and Agriculture Organization
4. de Moura MFSF, Silva MAL, de Morais AB, Morais JJL (2006) Equivalent crack based mode II fracture characterization of wood. Eng Fract Mech 73(8):978–993
5. Vasic S, Smith I (2002) Bridging crack model for fracture of spruce. Eng Fract Mech 69(6):745–760
6. de Borst R (2003) Numerical aspects of cohesive-zone models. Eng Fract Mech 70(14):1743–1757
7. de Moura MFSF, Morais JJL, Dourado N (2008) A new data reduction scheme for mode I wood fracture characterization using the double cantilever beam test. Eng Fract Mech 75(13):3852–3865
8. Silva F, Xavier J, Pereira FAM, Morais J, Dourado N, de Moura MFSF (2013) Determination of cohesive laws in wood bonded joints under mode I loading using the DCB test. Holzforschung 67 (8): 913-922
9. Fernberg SP, Berglund LA (2001) Bridging law and toughness characterisation of CSM and SMC composites. Compos Sci Technol 61(16):2445–2454
10. Xavier Xavier, J.; Oliveira, J.; Monteiro, P.; Morais, J.J.L.; de Moura, M.F.S.F. (2014) Direct evaluation of cohesive law in mode I of Pinus pinaster by digital image correlation. Experimental Mechanics (in press DOI: 10.1007/s11340-013-9838-y).

11. van den Bosch MJ, Schreurs PJG, Geers MGD (2006) An improved description of the exponential Xu and Needleman cohesive zone law for mixed-mode decohesion. Eng Fract Mech 73(9):1220–1234
12. Sutton M, Orteu J-J, Schreier H (2009) Image correlation for shape, motion and deformation measurements: Basic concepts, theory and applications. Springer
13. Sousa AMR, Xavier J, Morais JJL, Filipe VMJ, Vaz M (2011) Processing discontinuous displacement fields by a spatio-temporal derivative technique. Opt Laser Eng 49(12):1402–1412
14. Xavier J, Sousa AMR, Morais JJL, Filipe VMJ, Vaz M (2012) Measuring displacement fields by cross-correlation and a differential technique: experimental validation. Opt Eng 51, 043602
15. Xavier JC, Garrido NM, Oliveira M, Morais JL, Camanho PP, Pierron F (2004) A comparison between the Iosipescu and off-axis shear test methods for the characterization of Pinus pinaster Ait. Compos Part A-Appl S 35(7–8):827–840
16. Xavier J, Avril S, Pierron F, Morais J (2007) Novel experimental approach for longitudinal-radial stiffness characterisation of clear wood by a single test. Holzforschung 61(5):573–581
17. Xavier J, Oliveira M, Morais J, Pinto J (2009) Measurement of the shear properties of clear wood by the Arcan test. Holzforschung 63(2):217–225
18. GOM mbH. ARAMIS commercial software, ARAMIS 6.0.2; 2007.
19. Xavier J, de Jesus AMP, Morais JJL, Pinto JMT (2012) Stereovision measurements on evaluating the modulus of elasticity of wood by compression tests parallel to the grain. Constr Build Mater 26(1):207–215
20. Vasic S, Smith I (2002) Bridging crack model for fracture of spruce. Eng Fract Mech 69(6):745–760
21. Pereira JLE (2005) Comportamento mecânico da madeira em tracção nas direcções de simetria material. Msc thesis, University of Trás-os-Montes a Alto Douro, Vila Real (in Portuguese)

ACKNOWLEDGEMENTS

This work is supported by European Union Funds (FEDER/COMPETE - Operational Competitiveness Programme) and by national funds (FCT - Portuguese Foundation for Science and Technology) under the project FCOMP-01-0124-287 FEDER-022692. The authors would like to acknowledge the support of FCT under the project PTDC/EME-PME/114443/2009 and Ciência 2008 program.

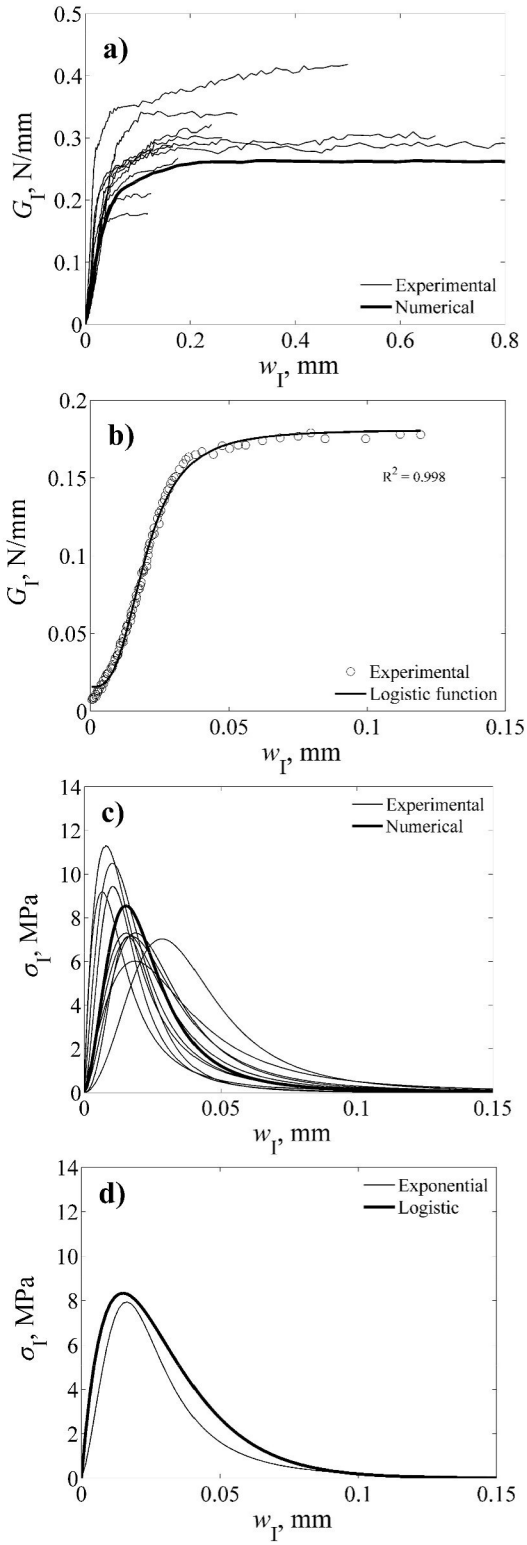

Fig. 4. DCB test processed by CBBM: (a) characteristic R–curves $(G_I - w_I)$; (b) least-square regression with the logistic function; (c) cohesive laws in mode I $(\sigma_I - w_I)$; (d) comparison between logistic and exponential mean cohesive laws.

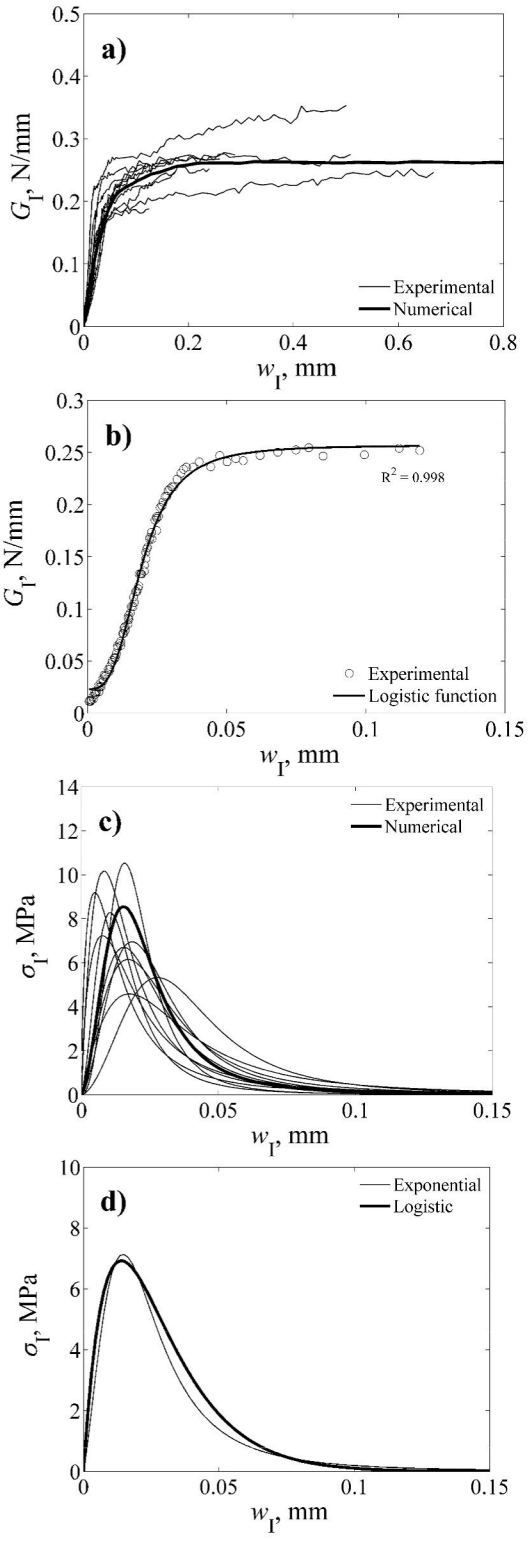

Fig. 5. DCB test processed by Irwin-Kies equation: (a) characteristic *R*–curves $(G_I - w_I)$; (b) least-square regression with the logistic function; (c) cohesive laws in mode I $(\sigma_I - w_I)$; (d) comparison between logistic and exponential mean cohesive laws.

Table 2. Parameters of the logistic function (A_1, A_2, p and $w_{I,0}$), and characteristic values of maximum stress (σ_{Iu}) and relative displacements (w_{Iu}, w_{Ic}, see Fig. 2) determined by CBBM.

Specimens	A_1	A_2	p	$w_{I,0}$	w_{Iu}	w_{Ic}	σ_{Iu}	
							Logistic	Exponential
	(N/mm)	(N/mm)	(-)	(mm)	(mm)	(mm)	(MPa)	(MPa)
1	0.016	0.35	2.45	0.026	0.018	0.12	9.19	9.16
2	0.011	0.29	2.05	0.017	0.010	0.12	10.5	9.90
3	0.016	0.18	3.09	0.020	0.016	0.08	7.14	5.49
4	0.005	0.28	2.43	0.027	0.019	0.13	7.31	6.37
5	0.016	0.30	2.21	0.027	0.017	0.15	7.16	6.52
6	0.004	0.29	1.81	0.016	0.008	0.12	11.3	11.2
7	0.006	0.21	2.40	0.015	0.010	0.08	9.44	8.32
8	0.013	0.31	1.99	0.032	0.019	0.19	6.02	5.71
9	0.019	0.35	2.81	0.037	0.029	0.16	7.04	5.60
10	0.004	0.25	2.24	0.024	0.015	0.13	7.30	6.61
Mean	0.011	0.28	2.35	0.024	0.016	0.13	8.24	7.48
C.V.[1] (%)	51.5	19.5	16.2	30.1	36.4	25.2	21.1	26.9

[1] Coefficient of variation (C.V.)

Table 3. Parameters of the logistic function (A_1, A_2, p and $w_{I,0}$), and characteristic values of maximum stress (σ_{Iu}) and relative displacements (w_{Iu}, w_{Ic}, see Fig. 2) determined by the Irwin-Kies equation.

Specimens	A_1	A_2	p	$w_{I,0}$	w_{Iu}	w_{Ic}	σ_{Iu}	
							Logistic	Exponential
	(N/mm)	(N/mm)	(-)	(mm)	(mm)	(mm)	(MPa)	(MPa)
1	0.001	0.32	1.51	0.014	0.005	0.14	9.19	9.81
2	0.002	0.23	1.60	0.019	0.008	0.14	7.20	7.45
3	0.023	0.26	3.15	0.019	0.016	0.08	10.5	8.00
4	0.005	0.25	2.48	0.026	0.019	0.13	6.95	6.01
5	0.013	0.26	2.14	0.027	0.017	0.15	6.15	5.69
6	0.004	0.26	1.82	0.016	0.008	0.12	10.2	10.0
7	0.005	0.18	2.37	0.015	0.010	0.08	8.28	7.35
8	0.009	0.25	1.86	0.033	0.018	0.18	4.58	4.38
9	0.013	0.27	2.64	0.038	0.028	0.16	5.33	4.38
10	0.004	0.23	2.24	0.024	0.014	0.13	6.70	6.06
Mean	0.008	0.25	2.18	0.023	0.014	0.13	7.51	6.93
C.V.[1] (%)	87.2	13.8	23.1	34.3	47.2	22.9	26.6	28.5

[1] Coefficient of variation (C.V.)